



**HAL**  
open science

# Synthesis of in situ purified iron nanoparticles in an electrochemical and vibrating microreactor: study of ramified branch fragmentation by oscillating bubbles

Audrey Iranzo, Fabien Chauvet

## ► To cite this version:

Audrey Iranzo, Fabien Chauvet. Synthesis of in situ purified iron nanoparticles in an electrochemical and vibrating microreactor: study of ramified branch fragmentation by oscillating bubbles. *Microfluidics and Nanofluidics*, 2019, 23 (3), pp.045. 10.1007/s10404-019-2211-4 . hal-02055893

**HAL Id: hal-02055893**

**<https://hal.science/hal-02055893>**

Submitted on 4 Mar 2019

**HAL** is a multi-disciplinary open access archive for the deposit and dissemination of scientific research documents, whether they are published or not. The documents may come from teaching and research institutions in France or abroad, or from public or private research centers.

L'archive ouverte pluridisciplinaire **HAL**, est destinée au dépôt et à la diffusion de documents scientifiques de niveau recherche, publiés ou non, émanant des établissements d'enseignement et de recherche français ou étrangers, des laboratoires publics ou privés.



## Open Archive Toulouse Archive Ouverte

OATAO is an open access repository that collects the work of Toulouse researchers and makes it freely available over the web where possible

This is an author's version published in: <http://oatao.univ-toulouse.fr/23143>

Official URL : <https://doi.org/10.1007/s10404-019-2211-4>

### To cite this version:

Iranzo, Audrey  and Chauvet, Fabien  *Synthesis of in situ purified iron nanoparticles in an electrochemical and vibrating microreactor: study of ramified branch fragmentation by oscillating bubbles.* (2019) *Microfluidics and Nanofluidics*. ISSN 1613-4982

Any correspondence concerning this service should be sent to the repository administrator: [tech-oatao@listes-diff.inp-toulouse.fr](mailto:tech-oatao@listes-diff.inp-toulouse.fr)

# Synthesis of in situ purified iron nanoparticles in an electrochemical and vibrating microreactor: study of ramified branch fragmentation by oscillating bubbles

Audrey Iranzo<sup>1,2</sup> · Fabien Chauvet<sup>1</sup> 

## Abstract

We report on a novel concept of microreactor for the synthesis of metal nanoparticles (nP). The principle is to make grow by electrocrystallization long metallic ramified branches, made of metal nanocrystals, in a Hele-Shaw cell. The activation of an integrated vibrating element (PZT disk) induces the fragmentation of these fragile branches and so the nanocrystal release. One advantage is the possibility to flush the branches (and so the nP), prior to fragmentation, to avoid purification step. This principle is applied here to the synthesis of iron nP and focus is put on the branch fragmentation. High speed visualisations highlight the key role of H<sub>2</sub> bubbles (co-formed during the branch growth). An effective fragmentation is obtained only using a square signal with which the initial bubbles coalesce. The resulting large bubbles exhibit shape oscillations and they induce microstreaming. This latter brings the branches close to bubble surface, where they are fragmented into fine particles. The required initial coalescence events are explained by a “dancing bubbles” effect made easier to achieve because initial small bubbles are excited at their resonance frequency by the sufficiently stiff signal steps. Transmission electron microscopy (TEM) reveals that dendritic particles,  $\sim 2 \mu\text{m}$  long and  $\sim 1 \mu\text{m}$  wide (broken secondary dendrites) with very high specific surface, and needle-like particles,  $\sim 200 \text{nm}$  long and  $\sim 20 \text{nm}$  in diameter (broken tertiary dendrites), are produced. A force balance, between the mechanical constraint applied by the fast flow near bubble surface and the material resistance, allows highlighting the key role of shape oscillations in the breakage of the dendrites.

**Keywords** Metal nanoparticles · Electrocrystallization · Microreactors · Bubble oscillations · Microstreaming · Fragmentation

## 1 Introduction

Metal nanoparticles (nP) attract significant interest mainly because of their optical (Fedlheim and Foss 2001; Kelly et al. 2003) and catalytic properties (Cuenya 2010). They are involved in various fields: biomedical applications [drugs vectorization by Au nP (Boisselier and Astruc 2009), Fe nP used as contrast agents in magnetic resonance imaging and in the treatment of tumours by hyperthermia (Hadjipanayis et al. 2008), etc.], heterogeneous catalysis [Pt and Pd nP in organic syntheses (Astruc et al. 2005) and fuel cells] and in environmental remediation [dechlorination, nitrate and heavy metals removal by Fe and Pd/Fe core-shell nP (Zhang 2003; Crane and Scott 2012)].

The optical and catalytic (reaction rate and selectivity) properties depend strongly on the size and the shape of the metal nP (Murphy et al. 2007; Cheong et al. 2010). Therefore, efficient synthesis methods to produce monodisperse

✉ Fabien Chauvet  
fabien.chauvet@univ-tlse3.fr

Audrey Iranzo  
A.Iranzo@tudelft.nl

<sup>1</sup> Laboratoire de Génie Chimique, Université de Toulouse, CNRS, INPT, UPS, Toulouse, France

<sup>2</sup> Present Address: Materials for Energy Conversion and Storage (MECS), Department of Chemical Engineering, Faculty of Applied Sciences, Delft University of Technology, Delft, The Netherlands

and shape-controlled metal nP are highly desirable. The most common synthesis method is the “colloidal” batch synthesis in which a reductant solution ( $\text{NaBH}_4$ , sodium citrate, etc.) is added, in a controlled manner, to a solution of the metal salt. Specific compositions (metal salt, type of reductant, surfactants/polymers to stabilize the particles) and conditions (temperature, mixing, flow rate, etc.) are determined, for a given metal, to (1) favour nucleation events and limit the growth of the particles and (2) produce particles with a controlled shape and a narrow size distribution [see, for example the batch synthesis of Fe nP (Wang and Zhang 1997)]. It has to be noted that, after the synthesis, a purification step is required to separate the produced nP from the remaining reacting species and by-products [dialysis, ion exchange resin, centrifugal or filtration processes (Sweeney et al. 2006)].

Nevertheless, this synthesis method suffers from weak reproducibility in size distribution and a slow screening capability (Marre and Jensen 2010). The use of microreactors, to carry out this synthesis continuously, has led to a significant progress in terms of screening capability, particle size distribution and control of particle shape. All of this is thanks to the high degree of control of mixing and transfers (hydrodynamics, mass and energy) in specifically elaborated microreactors (Song et al. 2008; Yang et al. 2010; Zhang et al. 2010; Marre and Jensen 2010; Ma et al. 2017). Two main types of microreactor have been employed: continuous flow-based and droplet-based microreactors.

In the work of Wagner et al. (2008), a continuous flow-based microreactor is used to synthesize Au and Ag nP; the metal precursor stream is mixed to the reductant stream in a passive micromixer, then the solution flows in a microchannel in which the growth, and thus the particle size, is controlled by the residence time. This configuration has two main drawbacks: (1) residence time distributions are often wide that prevents to obtain narrow particle size distributions (Song et al. 2008; Marre and Jensen 2010) and (2) clogging and particle adhesion on the internal walls can occur (Song et al. 2008; Ma et al. 2017).

With droplet-based microreactors, these drawbacks are avoided. The reactive mixture is confined in aqueous droplets which are transported along the microchannel by an oil phase [refer to the work of Duraiswamy and Khan (2009) for the synthesis of Au (rod-shaped) nP with this method]. However, these microreactors present the following drawbacks:

- the device materials (glass/silica, SU-8 resin based systems) and the fabrication are generally expensive (clean room facilities are required) (Ma et al. 2017)
- even if they are used in small quantities, the reductants (such as  $\text{NaBH}_4$ ) increase the production cost and are toxic, corrosive, and flammable (Wang et al. 2014)

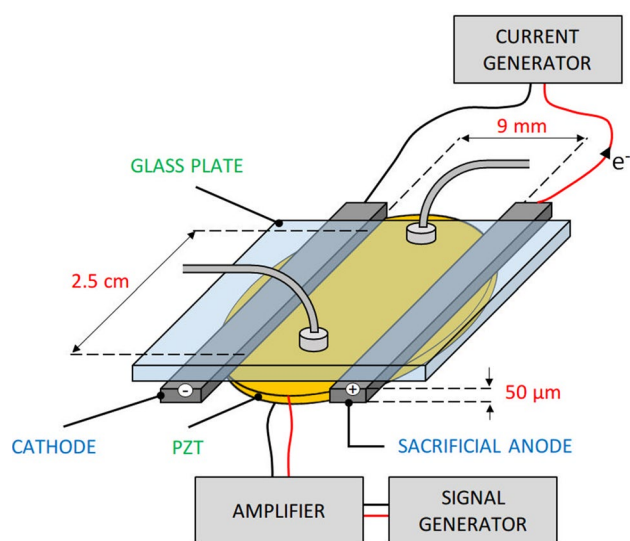


Fig. 1 Sketch of the electrochemical and vibrating microreactor

- a purification step is required as in batch synthesis (Ma et al. 2017).

Here, we propose the exploration of a new synthesis of metal nP in microreactor with the aim to overcome these drawbacks. The proposed method is based on the coupling of the direct electrochemical generation of metal particles (avoiding the use of reductant as  $\text{NaBH}_4$ ), in the form of “ramified branches”, from a simple and cheap aqueous metal salt solution, with their fragmentation, by the action of low-frequency acoustic vibrations, releasing the particles. The fabrication of the designed “electrochemical and vibrating” microreactor does not require clean room facilities. It consists in the assembly of two thin ( $50\ \mu\text{m}$ ) metal plates (the electrodes) between a piezoelectric disk (PZT, resonance frequency of 4 kHz) and a glass plate, see the sketch shown in Fig. 1. The formation mechanism of the ramified branches has already been explained in many works [see for example (Iranzo et al. 2017)] and it is briefly recalled here. The ramified branches are formed by galvanostatic electrolysis of the stagnant metal salt aqueous solution inside the microchannel. The constraint of electroneutrality forces the deposit to grow rapidly in the form ramified branches [growth velocity is equal to the velocity of the anions (Fleury 1997)]. These last grow by successive nucleation/growth events that leads to a fine branch structure made up of metal crystals whose can be nanometric and their size depends on the applied current density (Fleury 1997). This leads to the expectation of an external control of the produced nP in terms of size. The particles of interest are thus immobilized inside the microchannel, allowing them to be flushed by a simple flow of water (deionized and deaerated), before their fragmentation, to avoid subsequent purification steps.

The proposed method is applied here for the production of Fe nP from  $\text{FeCl}_2$  as an electrolyte. In such a thin gap cell, the growth of Fe branches is known to be accompanied by the formation of  $\text{H}_2$  bubbles due to the co-reduction of  $\text{H}^+$  (Bodea et al. 1999; Grujicic and Pesic 2005; Iranzo et al. 2015). The influence of the operating parameters (applied current and concentration of  $\text{FeCl}_2$ ) on the obtained deposit morphology (spatial arrangement of Fe branches and  $\text{H}_2$  bubbles) and the microstructure of the branches, in the proposed microreactor design, has already been studied and optimal conditions have been determined (Iranzo et al. 2017). The purity of the produced final solution (mass fraction of the metallic iron) has been estimated at  $\sim 83\%$ , that is well higher than the typical purity at the end of a colloidal synthesis  $\sim 10\%$  (Iranzo et al. 2017). The resulting deposit consists of an arrangement of long and parallel branches each one being surrounded by bubbles.

During the activation of the integrated PZT, the co-formed bubbles are expected to oscillate in such a way that they induce sufficiently fast fluid flows that fragment the branches and release the smaller particles that they are composed of. Indeed, when a bubble is subjected to a sound wave, with a frequency  $f$  close to its resonance frequency  $f_r$ , its oscillations induce a stationary and asymmetric flow (called acoustic streaming) in the liquid over a distance of the order of the bubble size (Tho et al. 2007; Rallabandi et al. 2014). In microfluidic systems, oscillating bubble-induced flows have been implemented, essentially to enhance the mixing (Liu et al. 2002; Wang et al. 2009; Ahmed et al. 2009). Furthermore, in close vicinity to the interface, fast oscillating flows are also generated due to the bubble surface motion itself; this has been used for example to fragment dendrites under ultrasonic cavitation (Shu et al. 2012).

This study focuses on the fragmentation of ramified Fe branches by oscillating co-formed bubbles. Fragmentation scenes are visualised with a high speed camera for several conditions of vibrations: with variation of the amplitude, the frequency and the waveform of the signal sent to the PZT. The corresponding behaviour of the bubbles (motions and coalescence, oscillation modes) is described and analysed with the support of theoretical considerations on both bubble shape oscillations and the “dancing bubble” effect. The fragmentation mechanism is studied comparing the structure of the branches, before fragmentation, to the produced particles (size distribution and TEM observations). The role of bubble oscillation on the fragmentation of the metallic branches is considered using a force balance between the mechanical stress and the mechanical resistance of the material. Finally, improvements of this method are discussed, as well as, the possible extension to other metals.

## 2 Experimental set-up and methods

### 2.1 The electrochemical and vibrating microreactor

The description of the electrochemical and vibrating microreactor can be found in (Iranzo et al. 2017); here, we detail it briefly. The microreactor used consists of two  $50\ \mu\text{m}$  thick iron plates, assembled in parallel between a glass plate and the PZT disk working in radial mode (lead/zirconate/titanate piezoelectric, resonance frequency = 4 kHz, capacitance = 20 nF, ABT-441-RC, Radiospare), see Fig. 1. The length of the electroactive zone is equal to 2.5 cm (Fig. 1). The assembly is held together using two clamps (not shown) that press on the glass plate and on the PZT.

### 2.2 Chemicals

The electrolytic solution ( $\text{FeCl}_2$  0.1 M) is prepared by dissolving  $\text{FeCl}_2 \cdot 4\text{H}_2\text{O}$  (99% Sigma-Aldrich) in deionized water ( $18.2\ \text{M}\Omega\text{-cm}$ ); no supporting electrolyte is used. This solution, and also the deionized water used to flush and to collect the particles, are deaerated (to prevent  $\text{O}_2$  co-reduction during the electrodeposition and to limit the Fe corrosion) by Argon bubbling during 15 min ( $\sim 30\ \text{mL}$ ) before being collected by a gastight syringe (Hamilton 1 mL, 1001LT) and injected into the microreactor. Experiments are achieved at room temperature ( $18\text{--}22\ ^\circ\text{C}$ ).

### 2.3 Instrumentation

A syringe pump (Harvard PHD 22/2000) is used for the injections of the solutions. The electrodeposition is driven by applying an electric current of 1 mA ( $80\ \text{mA}/\text{cm}^2$ ) between the electrodes using a potentiostat (Autolab PGSTAT100N). The PZT is activated by an electric signal generated by a function generator (GF467AF, Radiospare) and amplified by a Falco WMA-300 amplifier. The fragmentation process is visualised by reflection using a fibre optic illuminator and a high speed camera (Photron APX/RS 3000) equipped with a 105 mm macro-objective.

### 2.4 Characterization

The structure of the Fe branches (before fragmentation) is observed by scanning electron microscopy (SEM) with a JEOL JSM 7100F TTLS or a JEOL JSM 7800F Prime-EDS. An automated morphological optical analyzer (Morphologi G3 Malvern  $\times 50$ ) is used to measure the wet particle size distribution up to the optical resolution limit. The produced

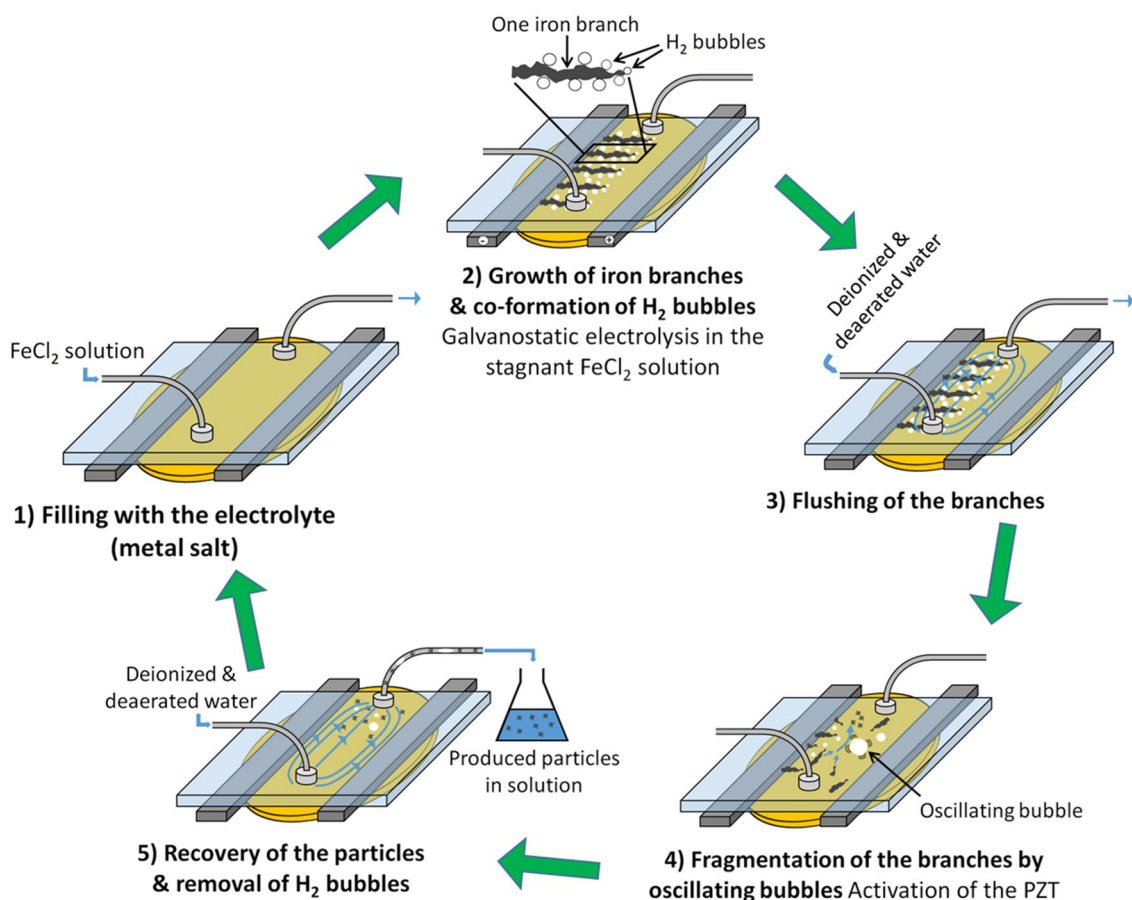


Fig. 2 Representation of the different phases of the synthesis

particles are also characterized by TEM with a JEOL JSM 2100F-EDS.

## 2.5 Description of the synthesis

The synthesis consists of five main phases (see Fig. 2):

- **Phase 1:** the microreactor is filled with the electrolyte ( $\text{FeCl}_2$  0.1 M).
- **Phase 2:** the current is applied, the branches start to grow on the cathode after a short depletion time ( $\sim 1$  s). The branches grow following a columnar morphology with a constant growth velocity;  $\text{H}_2$  bubbles nucleate and grow at the top of the branches and they are continuously left behind the moving front (Fig. 3a). It has to be noted that these bubbles, called *initial* bubbles from now, are not spherical but squeezed inside this thin cell since their apparent average diameter,  $114 \pm 30 \mu\text{m}$ , is higher than the cell depth ( $50 \mu\text{m}$ ). It has been previously shown (Iranzo et al. 2017) that only 5% of the applied current is used for the formation of these bubbles. The oxidation of the anode, made of iron, prevents the production of both

$\text{O}_2$  (bubbles never observed) and  $\text{Fe}^{\text{III}}$ . The electrolysis is stopped when the growth front reaches approximately the half the cell width (total duration  $\approx 300$  s). The branches thus formed consist of a dendritic structure exhibiting three levels of branching as shown in Fig. 3b. It has to be noted that this microstructure and its typical length scale have been observed on the entire analysed sample. This means that the same microstructure is continuously built during branches growth by galvanostatic electrolysis. This is of a great importance to produce particles with a narrow size distribution.

- **Phase 3:** the branches are flushed by a flow of deionized and deaerated water. A low flow rate,  $\sim 100 \mu\text{L}/\text{min}$ , is applied to avoid damaging the branches and displacement of the bubbles.<sup>1</sup> The residual concentration of  $\text{FeCl}_2$ , in the microreactor, depends on the duration

<sup>1</sup> The dissolution of the  $\text{H}_2$  bubbles is negligible because of both the low solubility of  $\text{H}_2$  in water ( $\sim 8 \cdot 10^{-4} \text{ mol/L}$ ) and the low surface area of the liquid-gas interfaces (the bubbles are squeezed in this confined geometry).

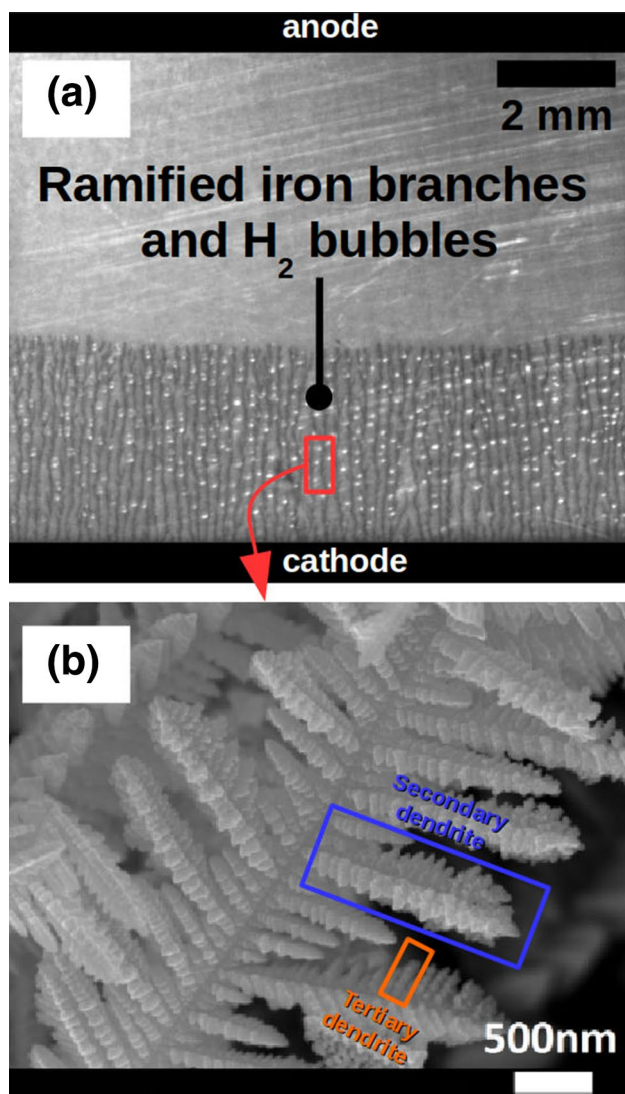


**Fig. 3** The ramified iron branches and the co-formed  $H_2$  bubbles generated by the galvanostatic electrolysis ( $FeCl_2$  0.1 M,  $80 \text{ mA/cm}^2$ , 300 s), **a** optical visualisation before the opening of the microreactor (centre of the microreactor), **b** observation of the structure of the branches by SEM

of the flushing; a duration of 10 min is used here (the corresponding total injected volume is equal to  $\sim 90$  times the volume of the microchannel).

- **Phase 4:** the PZT is activated during  $\sim 15$  s. The phenomena observed with the high speed camera are described in the following sections.
- **Phase 5:** a flow of deionized and deaerated water is applied to recover the particles and remove the bubbles.

These phases are repeated until the desired quantity of particles is collected.

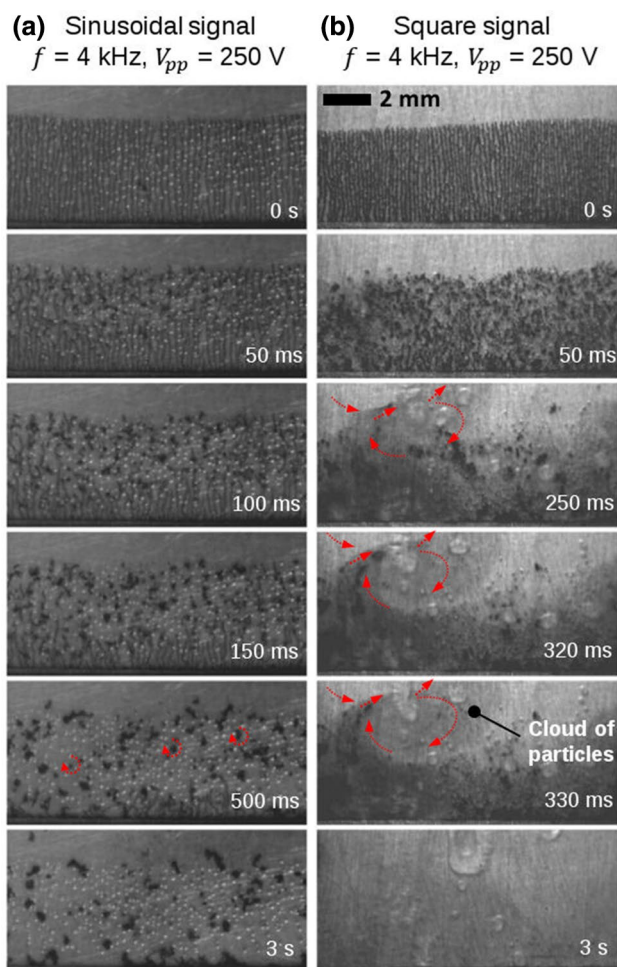


**Fig. 4** Image sequences of the fragmentation process for sinusoidal **(a)** and square **(b)** signals; the arrows indicate the observed particle motions;  $f = 4 \text{ kHz}$  and  $V_{pp} = 250 \text{ V}$ ; acquisition frequency = 1500 FPS, exposure time =  $1/1500 \text{ s}$

### 3 High speed visualisations of branch fragmentation and characterization of the produced particles

After the growth and the flush of the Fe branches, an amplified electric signal is sent to the PZT to induce the vibrations into the microreactor. Several experiments have been carried out varying the frequency  $f$  (100 Hz–4 kHz), the peak to peak voltage  $V_{pp}$  (120–250 V, after amplification) and the waveform (sinusoidal, triangular and square). The signal is symmetrical (centred on 0). The corresponding image sequences, acquired with the high speed camera (acquisition frequency = 1500 FPS, exposure time =  $1/1500 \text{ s}$ ), are shown in Figs. 4, 5 and 6. For all investigated cases, the pattern of the branches is strongly disturbed by the PZT activation.

The image sequence obtained using a sinusoidal signal (with  $f = 4 \text{ kHz}$  and  $V_{pp} = 250 \text{ V}$ ), Fig. 4a shows that the

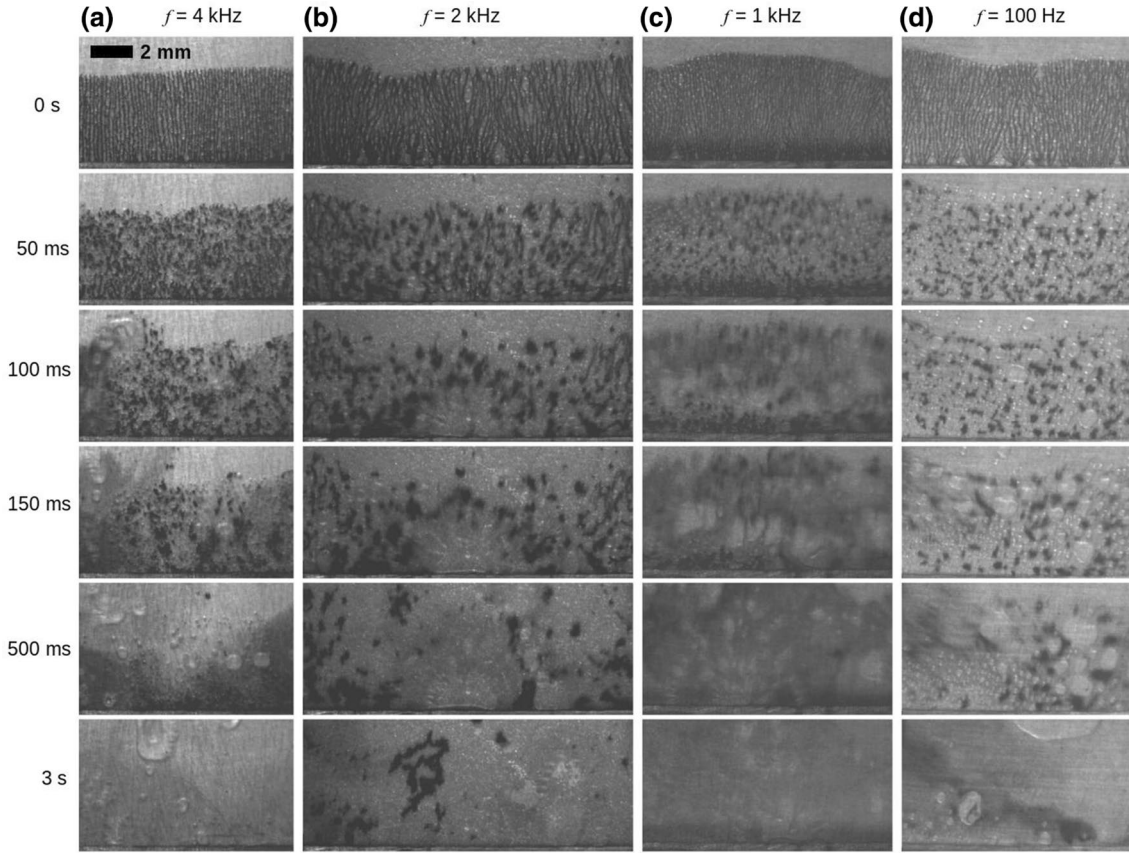


**Fig. 5** Image sequences of the fragmentation process for  $f = 4$  kHz (a),  $f = 2$  kHz (b),  $f = 1$  kHz (c) and  $f = 100$  Hz (d);  $V_{pp} = 250$  V; acquisition frequency = 1500 FPS, exposure time = 1/1500 s

branches are broken and the fragments are grouped into several blocks between the bubbles. Some blocks, not fully jammed between their neighbouring bubbles, are set in a stationary rotational motion in the plane of the channel (see the red arrows in Fig. 4a and the video in the supplementary information Frag\_Sin\_4kHz\_250V). These rotational motions are the signature of the expected bubbles microstreaming which is known to generate vortex flows (Liu et al. 2002; Tho et al. 2007). Nevertheless, these flows are not sufficiently fast to fragment the branches into small particles, even using the maximum value of  $V_{pp}$  of the examined range (as shown in Fig. 4a). It has to be noted that the bubble network is unaffected by the sinusoidal vibration of the PZT (no motions and no surface deformation). The fragmentation process, using a triangular signal (not shown), is similar to the one using a sinusoidal signal (branch breakage and block formation).

By performing the same experiment, but using a square signal instead of a sinusoidal signal (Fig. 4b), a more complex scene is visualised. Some of the initial bubbles (initially located between the branches) coalesce to form larger bubbles. The resulting bubbles exhibit surface deformations, splitting/coalescence events and motions inside the channel.

Microstreaming is also observed for the larger and unstable bubbles formed by coalescence (refer to the red arrows in Fig. 4b and the video in supplementary information Frag\_Sq\_4kHz\_250V). It is barely visible in the image sequence of Fig. 4b, but the initial bubbles (not still coalesced) generate also microstreaming as it can be clearly seen in Fig. 7. In this case, in a dedicated experiment, a single bubble, with a diameter  $\sim 100$   $\mu\text{m}$ , oscillates under a low amplitude (14 V) square signal. As when using a sinusoidal signal, flows arising from bubble microstreaming break the branches and put in motion the resulting fragments. Since the flows generated by the unstable large bubbles spread over larger areas than flows generated by the initial bubbles, the fragments end up being *attracted* to the surface of unstable bubbles where they are fragmented. This fragmentation process is visible in Fig. 4b where a group of branch fragments is “aspirated” by a large unstable bubble (exhibiting splitting/coalescence events). When they reach the surface of the corresponding split bubbles, they are fragmented and the ejection of a grey cloud is observed. This cloud is composed of particles that are too small to be visualised with the optical resolution used of 20  $\mu\text{m}$  (the size of one pixel on the images).

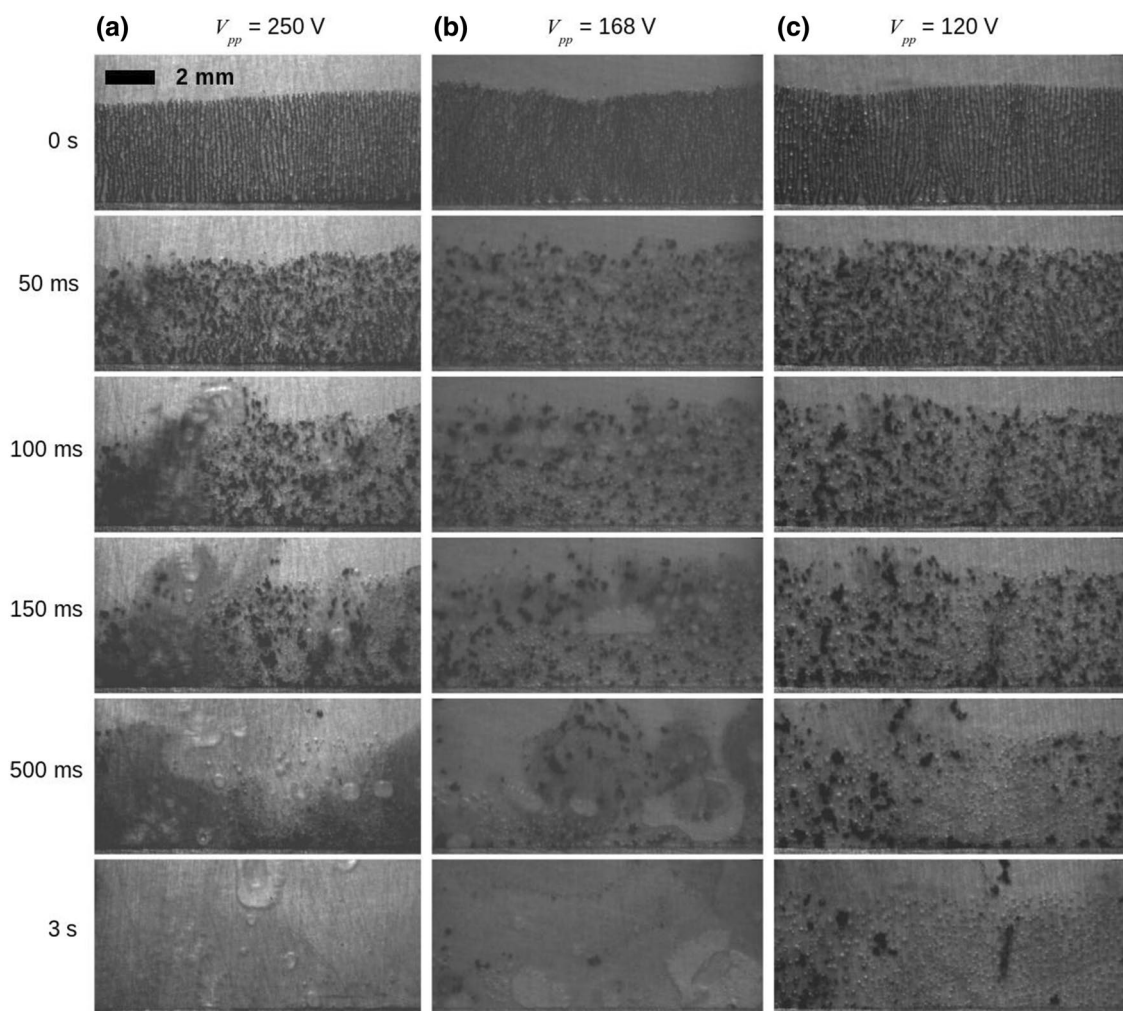


**Fig. 6** Image sequences of the fragmentation process for  $V_{pp} = 250$  V (a),  $V_{pp} = 168$  V, (b) and  $V_{pp} = 120$  V (c);  $f = 4$  kHz; acquisition frequency = 1500 FPS, exposure time = 1/1500 s

The wet particle size distribution (for  $f = 4$  kHz,  $V_{pp} = 250$  V and a square waveform) has been measured with an automated morphological optical analyser. The sample is a drop of the produced solution placed between two glass slides. The obtained distribution curve (Fig. 8) shows that the maximum particle size, in terms of circle equivalent diameter (based on the equivalent projected surface area), is effectively lower than  $20 \mu\text{m}$ . The shape of the curve suggests a significant amount of micrometric and submicrometric particles with a minimum size of less than the optical resolution limit  $\sim 500$  nm.

In Fig. 9, the TEM observations reveal two main types of particles:

- broken (Fig. 9a–d) and partially “plucked” dendrites (snatched secondary arms, Fig. 9c) whose length and width are, respectively,  $\sim 2 \mu\text{m}$  and  $\sim 1 \mu\text{m}$  for the examined samples; these dendrites are certainly secondary

dendrites detached from bigger primary dendrites as shown in Fig. 3b; their sphere equivalent specific surface,  $\sim 1.5 \times 10^8 \text{ m}^{-1}$  (from the estimation of the perimeter to surface ratio by image processing of Fig. 9b), corresponds to the specific surface of a spherical particle with a diameter of 40 nm

- small needle-like particles,  $\sim 200$  nm long and  $\sim 20$  nm in diameter, and other fragments whose shape is difficult to observe since they are superimposed and grouped into clusters (Fig. 9d–f); these nanometric fragments probably come from the fragmentation of the tertiary dendrites of the broken (secondary) dendrites described just before; the specific surface of these particles is  $\sim 2 \times 10^8 \text{ m}^{-1}$  that corresponds to a spherical particle with a diameter of 30 nm.

The size range of the broken dendrites corresponds to the decreasing part of the distribution curve for the particle sizes

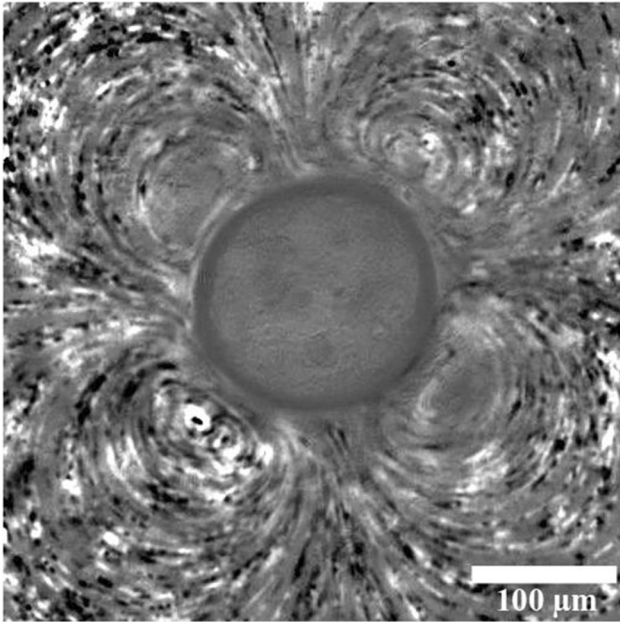
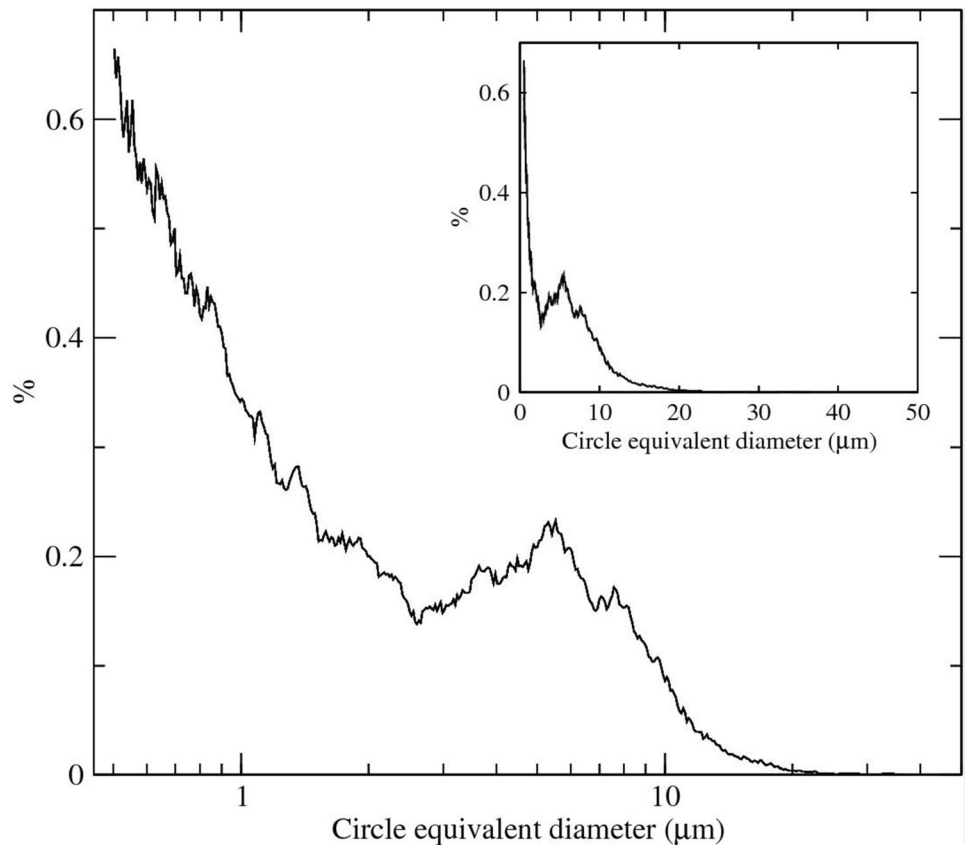


**Fig. 7** Microstreaming pattern obtained with an air bubble located in the centre of the channel and with a square signal ( $V_{pp} = 14$  V,  $f = 2$  kHz);  $5 \mu\text{m}$  polystyrene particles are used as tracers, superposition of recorded images for 2 s (1500 FPS)

$< \sim 2 \mu\text{m}$ . The other particles (needle-like particles and fragments) and/or agglomerates of them, even if they are too small to be optically resolved, appear as blur spots with sizes that could fall into the submicrometric range (due to light diffraction) and are then counted in the same size range. Concerning the biggest particles, up to  $\sim 10 \mu\text{m}$ , detected by the optical morphological analyser, they probably correspond to broken parts of primary dendrites as that, partially visualised, which appears to the right in Fig. 9a. Such “big” fragments are rarely encountered in the samples examined by TEM. This is in accordance with the relatively low occurrence frequency for this size range (Fig. 8). With the present data, it is not possible to estimate relative amounts of broken dendrites compared to needle-like particles. Nevertheless, these analyses provide useful information on the typical sizes of the fragmented particles that will be used below to elucidate the fragmentation mechanism.

To sum up, the fragmentation of the branches is observed only when large bubbles, formed by coalescence, oscillate with surface deformations under the action of the PZT driven with a square signal. This required particular behaviour is specifically analysed in the following section with the help of theoretical considerations on the bubble oscillation in this geometric configuration.

**Fig. 8** Size distribution in number of the produced particles driving the PZT with a square wave,  $f = 4$  kHz and  $V_{pp} = 250$  V. The inset corresponds to the same plot but with a linear scale for the  $x$ -axis; measurement realised from the produced particle dispersion (in water) with an automated morphological optical analyser (Morphologi G3 Malvern  $\times 50$ ), number of counted particles = 28,031



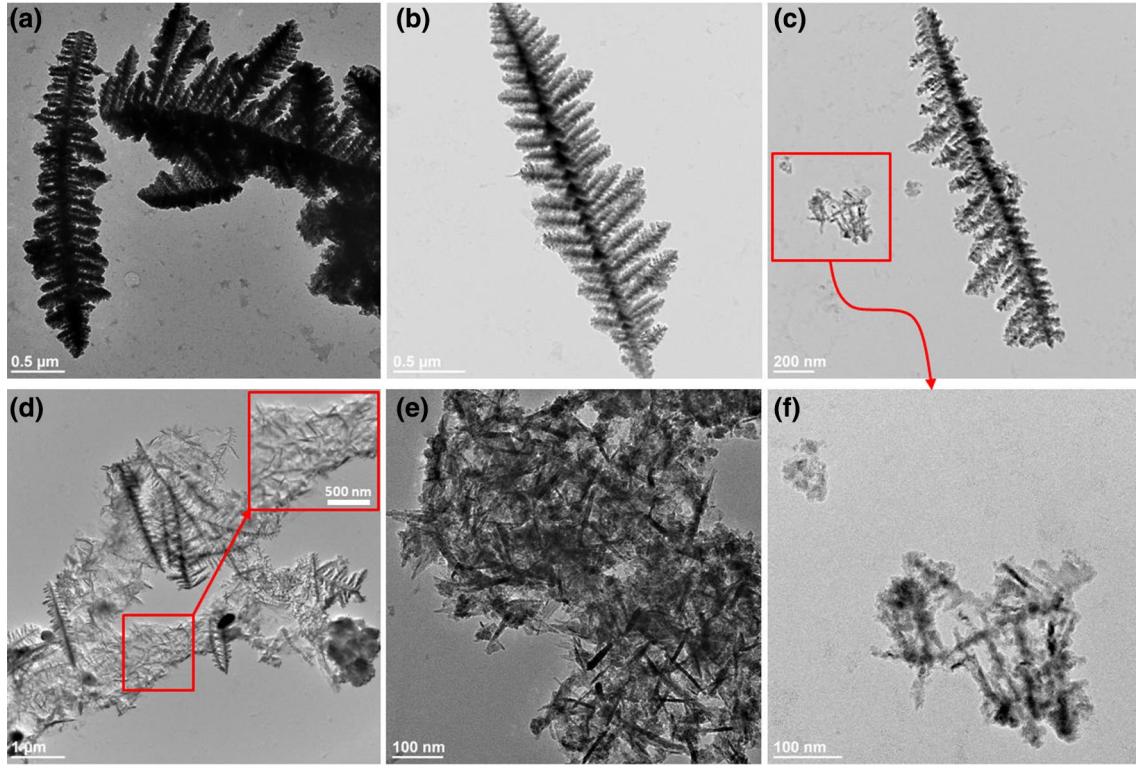


Fig. 9 TEM images of the produced particles,  $f = 4$  kHz and  $V_{pp} = 250$  V

Concerning the fragmentation, the dendrites (constituting the branches) are broken when the branches are brought to the surface of the unstable bubbles by microstreaming. Dendrites are broken at different levels: breakage of the primary dendrites, breakage of secondary dendrites at their roots and fragmentation of tertiary dendrites. In another section, these breakage events are also analysed considering the mechanical constraint acting on the dendrites (flow in the vicinity of the surface of the bubbles) and the material resistance (shear strength).

#### 4 On the coalescence of bubbles when the PZT is driven with a square signal

The analysis of the recorded images, just after the activation of the PZT, shows that the first coalescence events are due to sudden motions of some initial bubbles, which rapidly end up in contact with other motionless bubbles, see Fig. 10. The resulting bubbles continue to move across the initial bubble network, coalescing with other bubbles. Such a bubble motion has never been observed when using a sinusoidal or triangular signal. Erratic motions of unconfined bubbles in an acoustic field have been reported when using high acoustic pressure amplitude. This phenomenon is sometimes called “dancing

bubbles” (Eller and Crum 1970). It has been shown that this motion is related to the interactions between different modes of shape oscillation (Eller and Crum 1970; Doinikov 2004). Shape oscillations appear when stabilizing effects (surface tension and viscous stress) can no longer dampen the growth of infinitesimal shape perturbations. This happens when the pressure amplitude exceeds a certain threshold which depends on the liquid and gas properties, the frequency of the acoustic signal  $f$  and the rest radius of the bubble  $R_0$  (Eller and Crum 1970). The derivation of the corresponding amplitude threshold, in terms of bubble oscillation amplitude  $C_t = \Delta R_t/R_0$  for each mode  $n$  ( $n$  corresponding to the number of “peaks” on the bubble surface), by stability analysis, has been performed in several works (Francescutto and Nabergoj 1978; Prosperetti 1984) for spherical and unconfined bubbles submitted to a sinusoidal acoustic signal:

$$\Delta R_t/R_0 = \frac{2}{n - 1/4} \frac{\beta_n}{\omega}, \quad (1)$$

where  $\omega = 2\pi f$  is the applied pulsation and  $\beta_n = (n + 2)(2n + 1)\mu/\rho R_0^2$  the damping parameter of the shape oscillations of the mode  $n$  ( $\mu$  being the dynamic viscosity and  $\rho$  the density of the liquid). The influence of the bubble size and of the frequency on  $\Delta R_t/R_0$  can be obtained

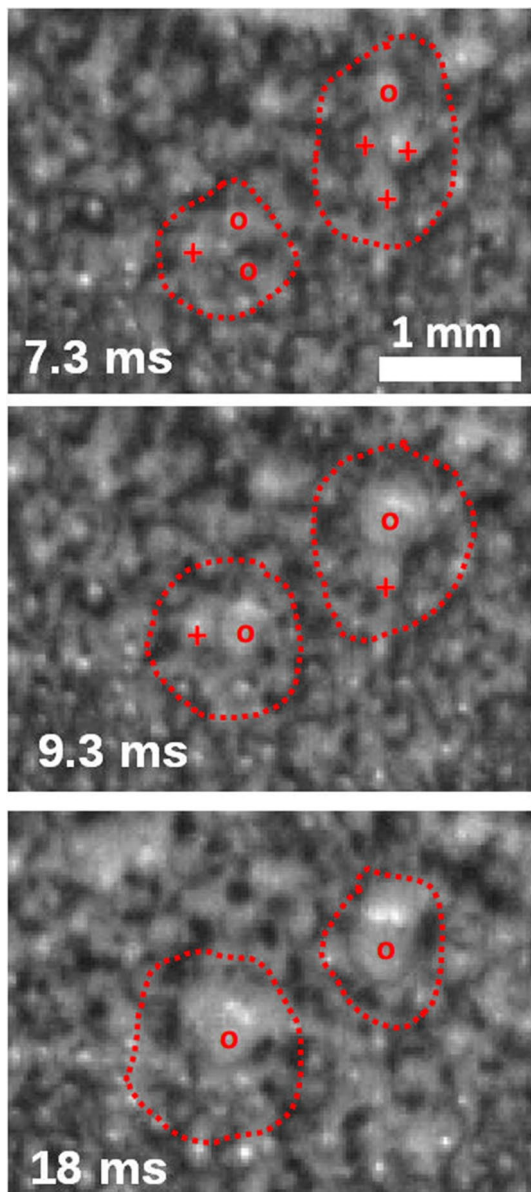


**Fig. 10** Image sequence showing some coalescence events. Circles and crosses indicate mobile and stagnant bubbles, respectively; square signal,  $f = 4$  kHz and  $V_{pp} = 168$  V; acquisition frequency = 1500 FPS, exposure time =  $1/1500$  s

using the fact that the most easily excitable mode  $n$  scales as  $R_0^{1/3}$  (in the limit of “large” values of  $n$ ):

$$\Delta R_t / R_0 \propto \frac{1}{R_0^{5/3} f_b}, \quad (2)$$

with  $f_b$  the oscillation frequency of the bubbles (corresponding to the applied frequency when a sinusoidal signal is used). Eq. (2) shows that, for a given  $f_b$ , large bubbles are less stable than small bubbles. This is attributed to the damping by viscous effect which is more important at small

scales. For a given  $R_0$ , the threshold decreases with  $f_b$ , as expected, since the growth rate of shape perturbations is directly related to  $f_b$  (Prosperetti 1984).

The observed motion of the initial bubbles in the microreactor could be explained by the same dancing bubble effect. To verify this assumption, it has to be shown that the bubble oscillation amplitude exceeds a certain threshold when using a square wave and not when using a sinusoidal or triangular wave.

Unfortunately, the prediction of  $C_t$  for unconfined and spherical bubbles, Eqs. (1)–(2), cannot be directly applied to the present situation. This is because the bubbles are not spherical, but squeezed and confined in the thin cell. In addition, instead of being exposed directly to an oscillatory pressure field (the cell depth of  $50 \mu\text{m}$  is well lower than the sound wavelength  $\approx 37$  cm here), the bubbles are subjected to the oscillation of the cell depth (bending of the surface of the PZT working in radial mode). Therefore, the driving force for the oscillation of the bubbles is the oscillatory cell depth instead of the oscillatory pressure field. This cell depth could be idealized as  $e(t) = e_0 + \epsilon(t)$  (neglecting side effects), with  $e_0$  the channel depth at rest ( $e_0 = 50 \mu\text{m}$ ).

However, in spite of these differences, by considering only the parameters related to the bubble oscillation ( $R_0$  and  $f_b$ ), and not the specific driving force, the dependence of both  $R_0$  and  $f_b$  on  $C_t$  should be the same as for a spherical bubble (Eq. 2). Indeed, even in this confined case, it is reasonably expected that the viscous damping should also increase when the bubble size decreases (the exponent of  $R_0$  in Eq. (2) may be different but still positive), and the shape perturbations should also be less damped when  $f_b$  increases. Consequently, for the present confined case, it is considered that the prediction of  $C_t$  (Eq. 1) applies in terms of scaling, Eq. (2).

It could be argued that the presence of the branches can disturb the oscillation of the bubbles which would prevent use of the proposed theory that was established for a simple liquid without particles. Indeed, such an effect is not expected here since the metallic branches are very porous. Indeed, one specific aspect of this kind of electrodeposit (the ramified branches) is that the concentration of metal inside each branch is very low. This is due to the “high” growth velocity (velocity of the anions) that forces the average density of the deposit to be very low and close to twice the electrolyte concentration (0.1 M), see (Léger et al. 2000). As a consequence, the branches should not disturb the oscillation of the bubbles.

Concerning the resonance frequency of such confined bubbles, Rabaud et al. (2011) found that  $f_t$  has an intermediate value between the resonance frequency for spherical bubbles  $f_r^{\text{sph}}$ , given by the Minnaert formula (Rabaud et al. 2011):

$$f_r^{\text{sph}} = \frac{1}{2\pi} \sqrt{\frac{3\sigma p_0}{\rho} \frac{1}{R_0}}, \quad (3)$$

and the resonance frequency for infinitely long cylindrical bubbles oscillating inside a liquid shell  $f_r^{\text{cyl}}$ , given by the work of Prosperetti (2004):

$$f_r^{\text{cyl}} = \frac{1}{2\pi} \sqrt{\frac{2}{\log(L/R_0)} \frac{\sigma p_0}{\rho} \frac{1}{R_0}}, \quad (4)$$

where  $\sigma$  is the polytropic exponent,  $p_0$  the static pressure and  $L$  the radius of the liquid shell. The results of Rabaud et al. (2011) suggest to consider:

$$f_r \approx \frac{f_r^{\text{sph}} + f_r^{\text{cyl}}}{2}. \quad (5)$$

Applying this last formula (Eq. 5) to the bubbles of interest, for which  $R_0 \approx 57 \mu\text{m}$ , using  $\sigma = 1$ ,  $\rho = 1000 \text{ kg/m}^3$  and  $L = 1 \text{ cm}$ , corresponding to the length scale of the lateral dimensions of the cell used ( $f_r^{\text{cyl}}$  depends slightly on  $L$  due to the slow increase of the logarithmic term),  $f_r \approx 33.1 \text{ kHz}$ .

Consequently, when a sinusoidal signal at 4 kHz is used, we are far from the resonance, and the pulsation amplitude  $\Delta R/R_0$  is expected to be very low. Experimental results suggest that even when using the maximum voltage amplitude of 250 V, the bubble pulsation amplitude is not high enough to induce shape deformations,  $\Delta R/R_0 < \Delta R_t/R_0$ .

Concerning the cases where a square signal is used, the oscillation of the initial bubbles, at  $f_r \approx 33.1 \text{ kHz}$ , could appear (free oscillation) during a plateau after a step, if the rise (and fall) time  $t_r$  of the steps of the channel depth signal  $e(t)$  is lower than  $1/(33.1 \text{ kHz}) = 30.2 \mu\text{s}$  (excitation of the bubbles at their resonance frequency). Thanks to an electric method described in the Appendix, it has been found that  $t_r$  is proportional to  $V_{\text{pp}}$ :  $t_r = 0.1 V_{\text{pp}}$  (with  $t_r$  given in  $\mu\text{s}$  and  $V_{\text{pp}}$  in volts).

Therefore,  $t_r$  is always lower than  $30.2 \mu\text{s}$  and so the initial bubbles are actually expected to oscillate at their resonance frequency after a step (a minimum number of 8.3 cycles is expected when 4 kHz is applied). Additionally, shape deformations are more likely to appear since from Eq. (2),  $\Delta R_t/R_0 \propto 1/f_b$  (the dependence on  $R_0$  is not considered here since the values of  $R_0$  are the same for the two analysed cases) is expected to be lower than when a sinusoidal signal at 4 kHz is used ( $f_b = 4 \text{ kHz}$ ). As a consequence, this analysis suggests that if the shape deformations (highlighted by coalescence events associated to the motions of the initial bubbles) occur for a given applied frequency using a square waveform, they should also occur for lower applied frequencies. This is indeed observed experimentally, as shown in Fig. 5, where coalescence events (and also the

fragmentation of the branches) appear for applied frequencies that range from 4 and 0.1 kHz and a voltage amplitude of 250 V. For a given applied frequency, it is expected that the pulsation amplitude  $\Delta R/R_0$  of the free oscillations should be proportional to the squeeze amplitude  $\Delta \epsilon$  which is itself proportional to the applied voltage amplitude. Consequently, below a threshold value of the applied voltage amplitude, no coalescence events should be observed. Once again, this is observed experimentally, as shown in Fig. 6, where the applied frequency is 4 kHz and the applied voltage varies between 250 and 120 V. The corresponding threshold value of  $V_{\text{pp}}$  is between 168 and 120 V.

The shape deformations of the initial bubbles are difficult to observe with both the magnification and the acquisition frequency (1500 FPS  $\ll$  33.1 kHz) used; the surface of the initial bubbles appears as blurred, which suggests a fast motion of the interface as expected. Shape deformations are more easily observed for slightly larger bubbles, from  $R_0 > \sim 200 \mu\text{m}$ . It is observed that the amplitude of the shape deformations increases with the bubble size. Additionally, fragmentation of the bubbles themselves (split/coalescence events), is even observed for the bigger ones (up to 1 mm in size). These observations suggest that the supercriticality  $(\Delta R/R_0)/(\Delta R_t/R_0) - 1$  increases with  $R_0$ . If the pulsation amplitude  $\Delta R/R_0$  is considered not dependent on  $R_0$  (it should mainly depend on the voltage amplitude),  $\Delta R_t/R_0$  should decrease when  $R_0$  increases. Such a trend is indeed expected from Eq. (2), from  $R_0 > R_0^{f=4 \text{ kHz}} = 511 \mu\text{m}$  (where  $R_0^f$  corresponds to the bubble size for which the resonance frequency, given by Eq. (5), is equal to the applied frequency  $f$ ), since in this case  $f_b$  is fixed and equal to the applied frequency  $f$ .

To sum up, the observed dynamics of the bubbles (coalescence and shape deformations), when a square signal is used, is explained by the onset of the oscillations of the bubbles at their resonance frequency after a sufficiently stiff step. A large enough voltage amplitude has to be applied to induce the coalescence of the initial bubbles and then all the bubbles are unstable and exhibit shape deformations. The branch fragmentation is analysed in the following section.

## 5 Branch fragmentation mechanism

It is observed that the fragmentation of the branches appears only when they are brought close to the surface of large bubbles formed by coalescence, exhibiting surface deformations (see the sketch in Fig. 11a). On the contrary, when no shape deformations are observed (use of a sinusoidal signal or a square signal without a sufficiently high applied voltage), the branches are only broken by the action of the microstreaming. The observed requirement of shape deformations to induce fragmentation is specifically analysed here.

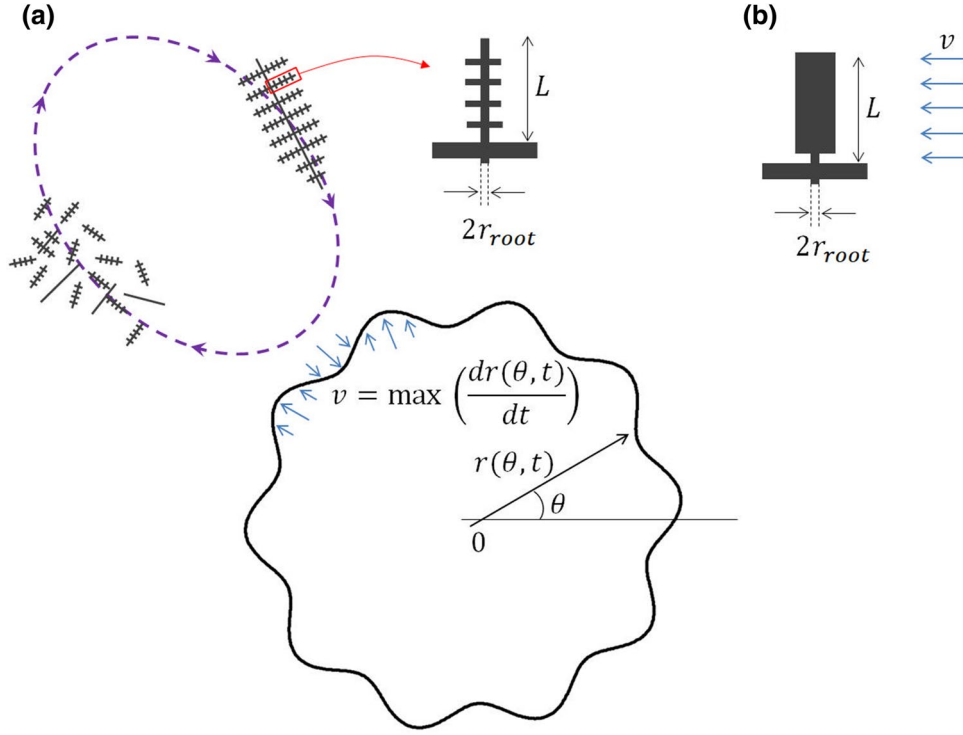


**Fig. 11** **a** Sketch of the fragmentation of the iron branches by a bubble oscillating with shape deformations (black closed line): the microstreaming (violet dash line) puts in motion the dendrites (grey), composing the branches, which end up bringing them close to the bubble surface where they are broken: the trunk of the primary dendrites is broken and the secondary dendrites are detached from the primary trunk, as sketched (the detachment of the tertiary dendrites from the secondary ones, as observed in Fig. 9d–f, is not sketched). **b** Equiva-

lent situation considered [inspired by (Shu et al. 2012)] to model a force balance, on the secondary dendrites, when the still unfragmented primary dendrites are in the vicinity of the bubble surface: a secondary dendrite is considered as a single rod, of length  $L$  and attached to a fixed wall (relative to the bubble surface displacement), subjected to a stationary flow of velocity  $v$  and perpendicular to the dendrite axis

We consider an overall and simplified force balance between the mechanical constraint applied on the dendrites (constituting the branches), in the vicinity of the surface of the bubbles, and the mechanical resistance of the dendrites. We use the same approach as in (Shu et al. 2012), where the mechanical constraint, originated from the surface displacement of a cavitation bubble, is assimilated to the viscous force acting on the secondary dendrites supposed to be attached to a fixed wall as sketched in Fig. 11b.<sup>2</sup>

<sup>2</sup> The use of this approach here implies that, the still unfragmented dendrites, arriving at the surface of the bubbles, are considered as immobile, compared to the vigorous oscillatory flow close to the bubble surface. Such a situation occurs, if the unfragmented branch piles (appearing as black blocks) are so heavy that, the time required for the matching between their displacement velocity and the oscillatory flow velocity, is well higher than the characteristic time of the oscillatory flow (around  $1/4000$  s). The estimation of this time is possible but difficult, mainly because the mass of a given branch pile is unknown. Indeed, the piles of branches could be more or less compressed during their transport by microstreaming, which complicates the estimation of their masses. However, this assumption is made here to enable, as a first approximation, the estimation of the mechanical stress acting on the secondary dendrites.

Assimilating the dendrite to a rod of length  $L$  connected to the wall by a smaller rod of radius  $r_{\text{root}}$  (Fig. 11b), Pilling and Hellawell (Pilling and Hellawell 1996) show that the stress  $\Sigma$ , generated by an uniform flow of velocity  $v$  perpendicular to the dendrite, is maximum at the dendrite root and it could be expressed as:

$$\Sigma = \frac{6\mu v L^2}{r_{\text{root}}^3}, \quad (6)$$

where  $\mu$  is the dynamic viscosity of the liquid.

The flow velocity  $v$  is assimilated to the maximum velocity of the bubble surface, see Fig. 11a.  $v$  has been measured for a given bubble size  $R_0 \approx 300 \mu\text{m}$  (typical size of the most destructive bubbles for  $f = 4$  kHz,  $V_{\text{pp}} = 250$  V), using very high speed visualisations (up to  $50 \times 10^3$  FPS, to be able to follow the surface displacement), for several values of the voltage amplitude. This has been done by first realising a typical experiment with  $f = 4$  kHz and  $V_{\text{pp}} = 250$  V. After the fragmentation phase, the solution is left in the cell and selected bubbles (with an equivalent radius  $\approx 300 \mu\text{m}$ )

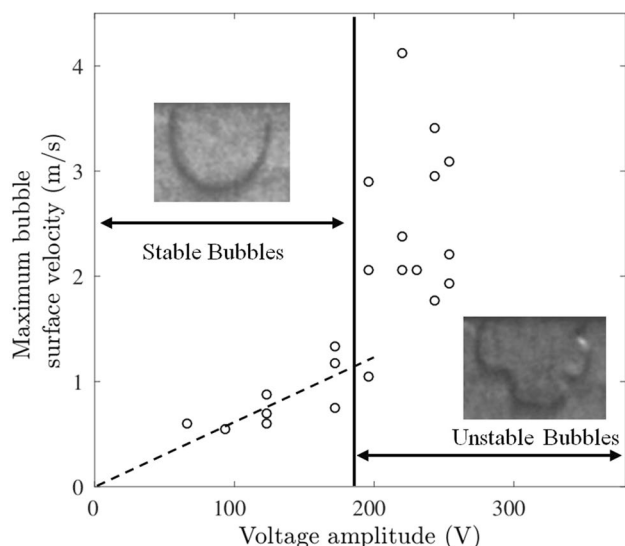


**Fig. 12** Maximum bubble surface velocity  $v$  measured for different bubbles, having a size  $R_0 \approx 300 \mu\text{m}$ , as a function of the voltage amplitude of the signal applied to the PZT ( $f = 4 \text{ kHz}$ ); these velocities are obtained measuring surface displacements on magnified visualisations of the bubbles such as the ones shown as insets and also using a very high acquisition rate ( $50 \times 10^3 \text{ FPS}$ )

are visualised to measure  $v$  varying the applied voltage. In Fig. 12, it is shown that below a threshold voltage  $\sim 190 \text{ V}$ , the bubbles oscillate without surface deformations and  $v$  is proportional to the voltage reaching  $\approx 1 \text{ m/s}$  when  $V_{pp} = 190 \text{ V}$ . For voltages higher than  $190 \text{ V}$ , the bubbles oscillate with surface deformations and  $v$  increases rapidly with  $V_{pp}$ , reaching up to  $4 \text{ m/s}$ .

Using the typical sizes of produced particles,  $L \sim 2 \mu\text{m}$  and  $r_{\text{root}} \sim 50 \text{ nm}$  for the broken secondary dendrites,  $L \sim 200 \text{ nm}$  and  $r_{\text{root}} \sim 10 \text{ nm}$  for the needle-like particles, and also the threshold velocity,  $\approx 1 \text{ m/s}$ , from which shape deformations appear, from Eq. (6), a failure stress  $\Sigma_f$  could be deduced for both kinds of produced particles (using  $\mu = 0.001 \text{ Pa}\cdot\text{s}$ ):  $\Sigma_f \sim 192 \text{ MPa}$  for broken dendrites,  $\Sigma_f \sim 240 \text{ MPa}$  for needle-like particles. A trend according to the size cannot be deduced because of the lack of precision of these measurements. Instead we retain a failure stress  $\sim 216 \text{ MPa}$  deduced from these experiments. This failure stress value has to be compared to the (ultimate) shear strength of material that the dendrites are composed of; the dendrites are supposed to be made of pure iron.

The shear strength is generally close to  $\sim 60$  to  $\sim 100\%$  of the (ultimate) tensile strength (Gargari 2005) which is the material property usually reported. From data available in (Lucon et al. 2015), the tensile strength of 99.9999878% pure bulk iron is around  $200 \text{ MPa}$ . Therefore, the deduced failure stress  $\sim 216 \text{ MPa}$  is of the same order of magnitude, and slightly higher, than iron shear strength which lies in the range  $\sim 120$  to  $\sim 200 \text{ MPa}$ .

This rather good matching allows the major role of bubble shape deformations to be highlighted. Bubble shape deformations induce a faster bubble surface displacement, and so a higher mechanical stress which allows the fragmentation of the metallic branches. Furthermore, it has to be noted that these unstable bubbles, in this system, are also able to break nano objects (the needle-like particles). Note that the mechanical constraint originated from the shear rate by the streaming flow, could also contribute to the fragmentation. The resulting stress could be estimated from  $\Sigma_{st} = \mu(v_{st}/l)$ , where  $v_{st}$  corresponds to the scale of the velocity of the streaming flow and  $l$  to the characteristic size of the shear zones. Near the bubble surface, the maximum expected value of  $\Sigma_{st}$  is  $\sim 80 \text{ Pa}$ , using  $v_{st} = 4 \text{ m/s}$  and  $l = 50 \mu\text{m}$  (shear across the cell thickness). This last value is well lower than the required constraint to break the dendrites which shows that the streaming flow is not responsible for the branch fragmentation.

## 6 Conclusion

To conclude, the proposed electrochemical and vibrating microreactor offers three main advantages compared to the colloidal synthesis in microreactors:

- in situ purification of the produced particles taking advantage of the immobilization of particles in the branches before fragmentation. The purity of the produced solution (mass fraction of the metallic iron) is estimated at  $\sim 83\%$  (Iranzo et al. 2017)
- the device is simple to assemble (clean room facilities are not required) and cost-effective (simple parts, low-frequency PZT and instrumentation)
- the only chemical used is the metal precursor, no reductants (and surfactants/polymers) are required
- the shape oscillation of the squeezed bubbles generates sufficiently high mechanical constraint to pull nanometric metal fragments ( $\sim 200 \text{ nm} \times \sim 20 \text{ nm}$ ). This observation is very important because it shows that it is possible to act mechanically on nanometric structures with the proposed device and that the proposed principle is valid.

The two main drawbacks are:

- a large particle size distribution
- a perfectible selectivity in terms of particle shape (dendritic and needle-like particles).

These drawbacks are mainly due to a lack of control of the fragmentation process, since the formation of the particles is well controlled during the branch columnar growth. It has been clearly observed that the branches are

fragmented by oscillating bubbles of different sizes which should induce different mechanical constraints on fragments of dendrites. This results in produced particles in the form of broken dendrites of different levels and sizes. A better control of the fragmentation process should be obtained using one bubble (or several bubbles of the same size) with a fixed and controlled location. This could be realised by integrating a microfluidic device for a controlled generation of bubbles (T-junction, flow focusing...) and also using bubble traps in the cell. This integration is indeed required if, for the targeted metal, the electrochemical formation of the branches is not accompanied with the co-formation of H<sub>2</sub> bubbles.

Concerning the control of the particle shape, this is clearly related to the electrochemical growth. It is expected to reach the same degree of versatility, than for the colloidal synthesis, using surfactants/polymers, and/or specific salts (counter ions), to control the growth of the metallic nanocrystals. This work is in progress in our team.

**Acknowledgements** This study was supported by the MSR Graduate Research Fellowship and the authors would like to thank the Paul Sabatier University for funding the research. The authors are very grateful to M. L. de Solan-Bethmale and C. Rey Rouch (Laboratoire de Génie Chimique), S. Le Blond du Plouy and Laurent Weingarten (Centre de microcaractérisation Raimond Castaing) for SEM and TEM observations. We thank the FERMAT Federation for the loan of the high speed camera.

## Appendix: Estimation of the rise time of the depth fluctuations $\epsilon(t)$

The current  $I(t)$  flowing through the PZT is the sum of a capacitive current  $I_c(t) = c_0 dV/dt$  ( $c_0$  being the capacitance and  $V$  the voltage at the PZT terminals) and a current  $I_p(t)$ , relative to the (direct and reverse) piezoelectric effect  $I_p(t) \propto dS/dt$ ,  $S$  being the strain of the PZT material (Arnau 2008) considered as an average value here. The derivation of the proportionality factor requires the integration of the fundamental piezoelectric relations considering the bending of the PZT disk and the metallic support as well as the location of the clamps. Here, we restrict the analysis and simply consider that the PZT surface bending, measured by  $\epsilon(t) = e(t) - e_0$ , is proportional to  $S$ ,  $I_p(t)$  is thus  $\propto de/dt$ . Consequently, from the simultaneous measurements of  $V(t)$  and  $I(t)$  and knowing (or measuring) the value of  $c_0 = 20$  nF, the form of the idealized depth fluctuations signal can be determined:  $e(t) - e_0 \propto \int_0^t (I(\tau) - I_c(\tau)) d\tau$ .

For the square signals, these measurements (with a filled cell) have shown that the PZT surface displacement is limited by the PZT response and a rise time  $t_r = 0.1V_{pp}$

(with  $t_r$  given in  $\mu$ s and  $V_{pp}$  in volts) has been determined (the rise time of the amplifier = 0.0005  $\mu$ s/V in open loop).

## References

- Ahmed D, Mao X, Shi J, Juluri BK, Huang TJ (2009) A millisecond micromixer via single-bubble-based acoustic streaming. *Lab Chip* 9(18):2738–2741
- Arnau A (2008) Piezoelectric transducers and applications. Springer, Berlin Heidelberg
- Astruc D, Lu F, Aranzaes JR (2005) Nanoparticles as recyclable catalysts: the frontier between homogeneous and heterogeneous catalysis. *Angew Chem Int Edn* 44:7852–7872
- Bodea S, Vignon L, Ballou R, Molho P (1999) Electrochemical growth of iron arborescences under in-plane magnetic field: morphology symmetry breaking. *Phys Rev Lett* 83(13):2612–2615
- Boisselier E, Astruc D (2009) Gold nanoparticles in nanomedicine: preparations, imaging, diagnostics, therapies and toxicity. *Chem Soc Rev* 38:1759–1782
- Cheong S, Watt JD, Tilley RD (2010) Shape control of platinum and palladium nanoparticles for catalysis. *Nanoscale* 2(2045–2053):2045–2053
- Crane RA, Scott TB (2012) Nanoscale zero-valent iron: future prospects for an emerging water treatment technology. *J Hazard Mater* 211–212:112–125
- Cuenya BR (2010) Synthesis and catalytic properties of metal nanoparticles: Size, shape, support, composition, and oxidation state effects. *Thin Solid Films* 518:3127–3150
- Doinikov AA (2004) Translational motion of a bubble undergoing shape oscillations. *J Fluid Mech* 501:1–24
- Duraiswamy S, Khan SA (2009) Droplet-based microfluidic synthesis of anisotropic metal nanocrystals. *Small* 5(24):2828–2834
- Eller AI, Crum LA (1970) Instability of the motion of a pulsating bubble in a sound field. *J Acoust Soc Am* 47(3B):762–767
- Fedlheim DL, Foss CA (2001) Metal nanoparticles: synthesis, characterization, and applications. CRC Press, London
- Fleury V (1997) Branched fractal patterns in non-equilibrium electrochemical deposition from oscillatory nucleation and growth. *Nature* 390(6656):145–148
- Franciscutto A, Nabergoj R (1978) Pulsation amplitude threshold for surface waves on oscillating bubbles. *Acta Acust Unit Acust* 41(3)
- Gargari MT (2005) Strength design in aluminum: a review of three codes. ASCE Publications
- Grujicic D, Pesic B (2005) Iron nucleation mechanisms on vitreous carbon during electrodeposition from sulfate and chloride solutions. *Electrochim Acta* 50(22):4405–4418
- Hadjipanayis CG, Bonder MJ, Balakrishnan S, Wang X, Mao H, Hadjipanayis GC (2008) Metallic iron nanoparticles for MRI contrast enhancement and local hyperthermia. *Small* 4(11):1925–1929. <https://doi.org/10.1002/sml.200800261>
- Iranzo A, Chauvet F, Tzedakis T (2015) Influence of electrode material and roughness on iron electrodeposits dispersion by ultrasonification. *Electrochim Acta* 184:436–451
- Iranzo A, Chauvet F, Tzedakis T (2017) Synthesis of submicrometric dendritic iron particles in an electrochemical and vibrating Hele–Shaw cell: study of the growth of ramified branches. *Electrochim Acta* 250:348–358
- Kelly KL, Coronado E, Zhao LL, Schatz GC (2003) The optical properties of metal nanoparticles: the influence of size, shape, and dielectric environment. *J Phys Chem B* 107:668–677

- Léger C, Elezgaray J, Argoul F (2000) Internal structure of dense electrodeposits. *Phys Rev E* 61(5):5452–5463
- Liu RH, Yang J, Pindera MZ, Athavale M, Grodzinski P (2002) Bubble-induced acoustic micromixing. *Lab Chip* 2(3):151–157
- Lucon E, Abiko K, Lambrecht M, Rehmer B (2015) Technical Note (NIST TN)-1879. NIST Pubs
- Ma J, Lee SM, Yi C, Li C (2017) Controllable synthesis of functional nanoparticles by microfluidic platforms for biomedical applications—a review. *Lab Chip* 17:209–226
- Marre S, Jensen KF (2010) Synthesis of micro and nanostructures in microfluidic systems. *Chem Soc Rev* 39:1183–1202
- Murphy CJ, Gole AM, Hunyadi SE, Stone JW, Sisco PN, Alkilany A, Kinard BE, Hankins P (2007) Chemical sensing and imaging with metallic nanorods. *Chem Commun* 5:544–557. <https://doi.org/10.1039/b711069c>
- Pilling J, Hellawell A (1996) Mechanical deformation of dendrites by fluid flow. *Metall Mater Trans A* 27(1):229–232
- Prosperetti A (1984) Bubble phenomena in sould fields: part two. *Ultrasonics* 22(3):115–124
- Prosperetti A (2004) Bubbles. *Phys Fluids* 16(6):1852–1865
- Rabaud D, Thibault P, Raven JP, Hugon O, Lacot E, Marmottant P (2011) Manipulation of confined bubbles in a thin microchannel: drag and acoustic Bjerknes forces. *Phys Fluids*. <https://doi.org/10.1063/1.3579263>
- Rallabandi B, Wang C, Hilgenfeldt S (2014) Two-dimensional streaming flows driven by sessile semicylindrical microbubbles. *J Fluid Mech* 739:57–71
- Shu D, Sun B, Mi J, Grant PS (2012) A high-speed imaging and modeling study of dendrite fragmentation caused by ultrasonic cavitation. *Metall Mater Trans A Phys Metall Mater Sci* 43(10):3755–3766
- Song Y, Hormes J, Kumar CSSR (2008) Microfluidic synthesis of nanomaterials. *Small* 4(6):698–711
- Sweeney SF, Woehle GH, Hutchison JE (2006) Rapid purification and size separation of gold nanoparticles via diafiltration. *J Am Chem Soc* 128(10):3190–3197
- Tho P, Manasseh R, Ooi A (2007) Cavitation microstreaming patterns in single and multiple bubble systems. *J Fluid Mech* 576:191–233. <https://doi.org/10.1017/S0022112006004393>
- Wagner J, Tshikhudo TR, Köhler JM (2008) Microfluidic generation of metal nanoparticles by borohydride reduction. *Chem Eng J* 135:S104–S109
- Wang C, Zhang W (1997) Synthesizing nanoscale iron particles for rapid and complete dechlorination of TCE and PCBs. *Environ Sci Technol* 31(7):2154–2156
- Wang SS, Jiao ZJ, Huang XY, Yang C, Nguyen NT (2009) Acoustically induced bubbles in a microfluidic channel for mixing enhancement. *Microfluid Nanofluid* 6(6):847–852
- Wang T, Jin X, Chen Z, Megharaj M, Naidu R (2014) Green synthesis of Fe nanoparticles using eucalyptus leaf extracts for treatment of eutrophic wastewater. *Sci Total Environ* 466:210–213
- Yang S, Cheng F, Yeh C, Lee G (2010) Size-controlled synthesis of gold nanoparticles using a micro-mixing system. *Microfluid Nanofluid* 8(3):303–311
- Zhang W (2003) Nanoscale iron particles for environmental remediation: an overview. *J Nanopart Res* 5:323–332
- Zhang Y, Jiang W, Wang L (2010) Microfluidic synthesis of copper nanofluids. *Microfluid Nanofluid* 9(4):727–735

**Publisher's Note** Springer Nature remains neutral with regard to jurisdictional claims in published maps and institutional affiliations.